nature communications

Article

https://doi.org/10.1038/s41467-024-53953-4

Micro-homogeneity of lateral energy landscapes governs the performance in perovskite solar cells

Received: 15 February 2024

Accepted: 29 October 2024

Published online: 09 November 2024

Check for updates

Pengju Shi[1,2,3,10], Bin Ding[4,5,10], Donger Jin[1,10], Muratcan Oner[6,10], Xu Zhang[1,2,3], Yuan Tian[1,2,3], Yahui Li[1,2], Ke Zhao[1,2,3], Zengyi Sun[1], Jiazhe Xu[1,2,3], Shaochen Zhang[1,2,3], Runchen Lai[7], Lingyu Xiao[7], Chenyue Wang[8], Caner Değer[6], Liuwen Tian[1,2,3], Jiahui Shen[1,3], Yuan Cheng[7], Ilhan Yavuz[6], Xiaohe Miao[7], Enzheng Shi[2], Deren Yang[1], Yong Ding[4,9] ✉, Mohammad Khaja Nazeeruddin[4] ✉, Rui Wang[2,3] ✉ & Jingjing Xue[1] ✉

Suppression of energy disorders in the vertical direction of a photovoltaic device, along which charge carriers are forced to travel, has been extensively studied to reduce unproductive charge recombination and thus achieve high-efficiency perovskite solar cells. In contrast, energy disorders in the lateral direction of the junction for large-area modules are largely overlooked. Herein, we show that the micro-inhomogeneity characteristics in the surface lateral energetics of formamidinium (FA)-based perovskite films also significantly influence the device performance, particularly with accounting for the stability and scale-up aspects of the devices. By using organic amidinium passivators, instead of the most commonly used organic ammonium ones, the micro-inhomogeneity in the lateral energy landscapes can be suppressed, greatly improving device stability and efficiency of FA-based single-junction perovskite solar cells.

Constructed with vertical junctions, solar cells always target favored energetics in the vertical direction to ensure efficient carrier transport across the device. In perovskite solar cells (PSCs), great efforts have been made in this regard to confer flat energy landscapes with minimized electronic disorders across the junctions, resulting in high power conversion efficiencies (PCEs)[1–3]. Various techniques have been employed for this purpose, for instance, controlling crystal growth[4–8], compositional engineering[9–12], aligning energy bands[13–16], and surface passivation[16–19]. Among these techniques, surface passivation has recently become the most intensively studied and indispensable strategy for achieving stable and high-performance PSCs. Many chemicals have been investigated to passivate surface defects and thus reduce energy disorders along the carrier transport pathways vertically[20,21].

The mitigation of electronic disorders across the vertical junction has been extensively studied by developing various surface defect

[1]State Key Laboratory of Silicon and Advanced Semiconductor Materials, School of Materials Science and Engineering, Zhejiang University, Hangzhou, China. [2]Department of Materials Science and Engineering, School of Engineering, Westlake University, Hangzhou 310030, China. [3]Division of Solar Energy Conversion and Catalysis at Westlake University, Zhejiang Baima Lake Laboratory Co., Ltd, Hangzhou 310000 Zhejiang, China. [4]Group for Molecular Engineering of Functional Materials, Institute of Chemical Sciences and Engineering, EPFL VALAIS, Sion, Switzerland. [5]College of Chemistry, Chemical Engineering and Materials Science, Soochow University, Suzhou, P. R. China. [6]Department of Physics, Marmara University, Ziverbey, Istanbul 34722, Turkey. [7]Instrumentation and Service Center for Molecular Sciences, Westlake University, Hangzhou 310024 Zhejiang Province, China. [8]Shanghai Synchrotron Radiation Facility (SSRF), Zhangjiang Lab, Shanghai Advanced Research Institute, Chinese Academy of Sciences, 239 Zhangheng Road, Shanghai 201204, China. [9]Beijing Key Laboratory of Novel Thin-Film Solar Cells, North China Electric Power University, Beijing 102206, P. R. China. [10]These authors contributed equally: Pengju Shi, Bin Ding, Donger Jin, Muratcan Oner. ✉e-mail: dingy@ncepu.edu.cn; mdkhaja.nazeeruddin@epfl.ch; wangrui@westlake.edu.cn; jjxue@zju.edu.cn

passivation strategies, in which reducing the overall density of surface defects is the focus. However, surface lateral energy disorders, although detrimental to perovskite modules performance as well, have received less attention[22–24]. We now show that the surface lateral micro-homogeneity of the energy landscape governs the performance of PSCs, particularly with accounting for the stability and scale-up characteristics of the devices. We find that the most widely employed organic ammonium surface passivators, despite their benefits for suppressing electronic trap states across the junction, can cause microscopic inhomogeneity in the lateral energetics, compromising the stability of PSCs. In contrast, their organic amidinium counterparts can deliver homogeneous lateral energy landscapes at a microscopic level, which greatly improves the performances of PSCs and modules. The small-area device and solar module (27.2 cm^2) achieved champion aperture PCEs of 25.5% and 22.5% (active-area PCE of 23.4%, certified), respectively. The PSCs maintained 90% of their efficiency at 70 °C for around 6000 h, highlighting the significance of micro-homogeneity of lateral energy landscapes in affecting PSC performances.

Results

Micro-homogeneity of lateral energy landscapes

As the most widely reported surface passivators in PSCs, organic ammoniums feature a head unit of the prototypical A-site organic component in perovskites (chemical formula ABX_3), called methylammonium (MA^+). This series of molecules usually allows for effective surface passivation of perovskite by binding the ammonium head to the defective Pb-I framework[18,19,25]. The research attention has recently turned from MA-based perovskites to formamidinium (FA)-based ones for high-performance PSCs[26,27], which inspired us to explore the potentials of amidinium-based surface passivators. Amidinium-containing molecular structures have been used in a few earlier studies as additives in the perovskite precursors (mostly in MA-based perovskites) to control the bulk properties of perovskite thin films[28,29]. Their potentials and influences as surface passivators have yet to be fully explored and well understood[30–32]. Taking into accounts the same structural versatility of the amidinium passivators as their ammonium counterparts, the various units in the molecules may offer different functionalities and thus affect the surface properties as in the ammonium-based cases. Motivated by this, we compared a series of conventional organic ammonium passivators with the organic amidiniums ones in $FAPbI_3$-based PSCs. Two sets of molecular structures were chosen as prototypes, including alkyl chains and aromatic units applied as tethering groups—pentylammonium (PAm), pentylamidinium (PAd), phenylpropanylammonium (PPAm), and phenylpropanylamidinium (PPAd), the molecular structures of which are shown in Fig. 1A.

We solution-processed $FAPbI_3$-based perovskite films ($FA_xCs_{1-x}PbI_3$) using a two-step method with surface treatment of these organic ammonium and amidinium passivators, respectively. We first investigated the ensemble surface electronic energetics of the films using ultraviolet photoelectron spectroscopy (UPS). The high energy cutoff positions were approximately the same, suggesting the similar Fermi levels of the perovskite surfaces treated by different molecules (Supplementary Fig. 1). This indicated the comparable energy landscapes that affecting charge carrier behavior as they travel vertically across the junction (Supplementary Fig. 2). Despite the similarity in the averaged vertical electronic energetics, Kelvin probe force microscopy (KPFM) measurements revealed a difference in the spatially resolved lateral electronic features of these films (Supplementary Fig. 3). Inhomogeneous distributions of the Fermi levels on the microscale were observed on perovskite surfaces for PAm, PAd, and PPAm treatments, whereas PPAd treatment led to a smooth lateral energy landscape (Fig. 1B). In a more focused image of a typical perovskite grain for each case, we observed a generally higher surface potential of the grain than the grain boundary (Supplementary Fig. 4). However, the surface potential offsets between the grains and grain boundaries were significantly suppressed for PPAd. A statistical comparison of the potential offsets for all the cases further consolidated the reduced lateral electronic inhomogeneity in PPAd (Supplementary Fig. 5).

By comparing the molecular structures and their interaction with perovskites, we found that the structures of both the head and tail units influenced the microscale molecular distribution and thus the micro-homogeneity of lateral electronic energetics. We performed Fourier transform infrared spectroscopy (FTIR) measurements to study the interaction between the molecules and the PbI_2-terminated perovskite surfaces. C–N in pure PAm and PPAm showed typical stretching vibration modes at 1084 and 1059 cm^{-1}, respectively, which shifted to 1080 and 1058 cm^{-1} upon binding to PbI_2, respectively (Fig. 1C). More pronounced peak shifts of C=N were observed in amidiniums. The typical stretching vibration of C=N exhibited a downward peak shift reaching 26 and 17 cm^{-1} in PAd and PPAd, respectively, suggesting a stronger interaction between the amidinium head group and the Pb-I framework than the cases of ammoniums. This stronger interaction was attributed to the abundant hydrogen bonds afforded by the two N-H groups in amidiniums. The favorable chemical binding between amidiniums and the Pb-I framework was also evidenced by the readily formed low-dimensional perovskite phases with amidinium cations. Grazing-incidence wide-angle X-ray scattering (GIWAXS) measurements revealed the formation of low-dimensional perovskite phases on the surfaces of $FAPbI_3$-based perovskite films with the PAd and PPAd treatments, as indicated by the diffraction patterns at low q_z values (Supplementary Figs. 6 and 7).

To gain deeper insights into the structures led by different surface treatments, we managed to grow the single crystals of the low-dimensional perovskites with PPAm and PPAd, respectively. The crystal structures of the PPAm- and PPAd-based perovskites determined by the single-crystal analysis are displayed in Fig. 1D (the crystal data, structure refinement, and the atomic coordinates are shown in Supplementary Tables 1 and 2). The most energetically favorable phase derived from the PPAm was a layered 2D perovskite structure with continuous Pb-I framework in the in-plane direction. In contrast, PPAd delivered a 1D structure with disrupted Pb-I framework by stacked organic moieties in one of the dimensions. The reduced dimensionality and the flexible intermolecular interaction afforded by the soft organic contact could make it more readily to form the low-dimensional perovskite layer on the surface of the 3D perovskites. The soft organic contact via π–π interaction can help release the strain of the rigid Pb-I framework at the interface, and thus making it easier to achieve a full surface coverage.

This can be verified by the discrepancies in the diffraction patterns of the free-standing low-dimensional single crystal, low-dimensional polycrystalline thin film, and the low-dimensional layer grown on the surface of the 3D perovskite film. In the case of 3D perovskite film with PPAd atop, the main diffraction peak of the PPAd-based 1D phase located at 7.20° as extracted from the GIWAXS measurements. The peak position was highly consistent with that in the free-standing PPAd-based single crystal (7.17°) and the polycrystalline 1D thin films (7.22°), which suggested very small lattice strain when PPAd-based 1D phases formed atop (Supplementary Fig. 8). However, for the case of PPAm, large discrepancies were observed in the positions of the diffraction peaks derived from the 2D phases. The diffraction peak located at 5.36° and 4.56° for the single crystal and the thin film, respectively (the low-dimensional diffraction peak for the PPAm deposited on the 3D perovskite film was too small to be detectable in the GIWAXS measurements even with synchrotron-based light source, Supplementary Fig. 9). The large discrepancy in the diffraction peaks of the free-standing single crystal and the thin film suggested that large lattice strain may be induced when the PPAm-based 2D phases were grown on the surface, and thereby can lead to inhomogeneous surface coverage and disordered surface energy

https://doi.org/10.1038/s41467-024-53953-4

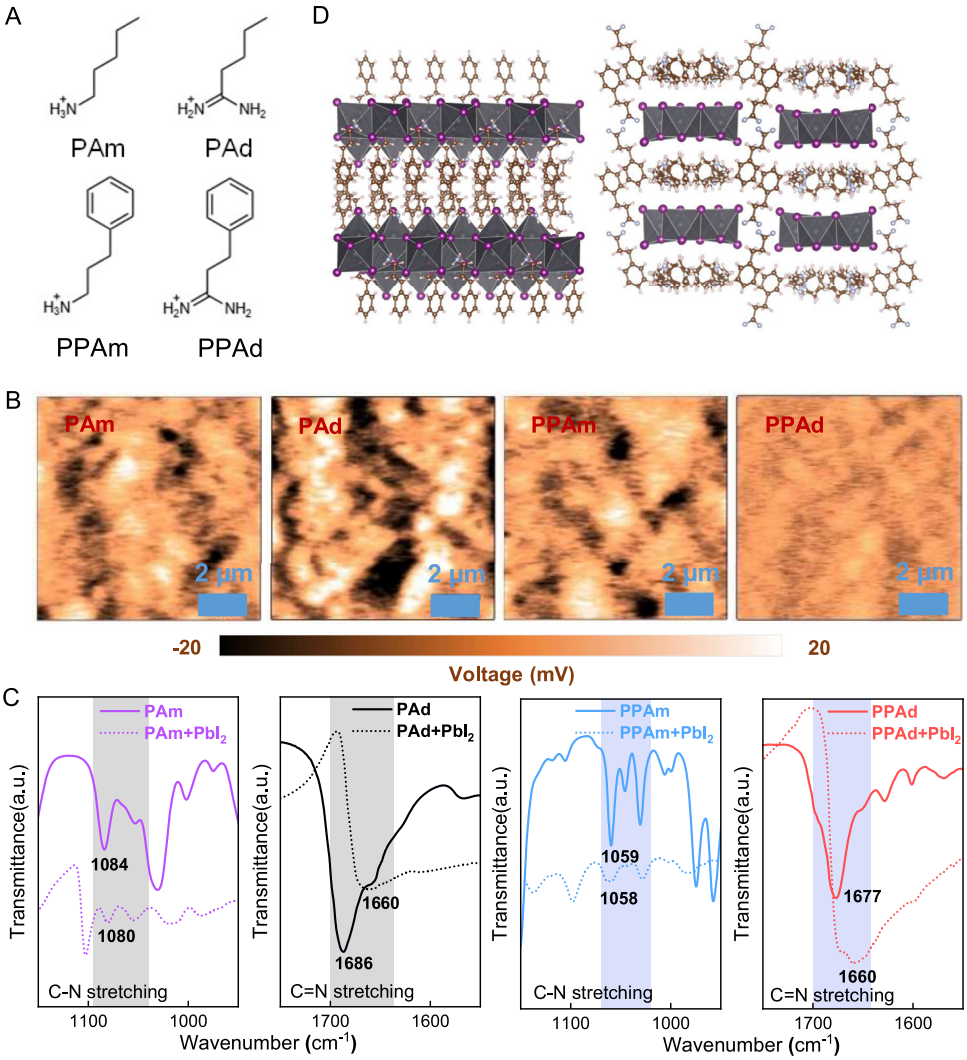

Fig. 1 | Micro-inhomogeneity of the lateral energy landscape in perovskite thin films. A Molecular structures of organic ammonium and amidinium passivators. **B** KPFM images of perovskite films treated with PAm, PAd, PPAm, and PPAd. **C** FTIR spectra of pure and PbI_2-bound PAm, PAd, PPAm, and PPAd. **D** Crystal structures of PPAd- and PPAm-based low dimensional perovskite phases.

landscape observed. The 1D phase is more easily formed on the surface than its 2D counterpart also evidenced the reduced interfacial strain that may serve as energy barrier for the crystallization. The influence of these two different structures on the surface features can also be reflected by the surface morphologies of the low-dimensional phases grown on atop of the 3D perovskite. The thickness of the 3D perovskite was reduced by decreasing the precursor concentration to 100 mM to magnify the influence of the surface treatment and better reflect the difference. As shown in Supplementary Fig. 10, the PPAm led to plate-like surface features on the topic of 3D perovskites, whereas PPAd led to dot-like surface features, which could more readily approach a fully covered and uniform surface landscape (Supplementary Fig. 11).

To further verify the more uniform distribution of the PPAd-derived 1D phase on the surface of perovskite film, we employed spectral analysis to unveil the surface distribution of the PPAd-based 1D phase on the 3D perovskite films. The characteristic PL emission of the low-dimensional perovskite phases were determined to be ~600 nm for both the PPAm and PPAd (Supplementary Fig. 12). Supplementary Fig. 13 showed the distribution of the PL signals collected at 600 nm, representing the characteristic signals from the PPAm and PPAd-based low-dimensional phases. The PL signal of the PPAd-based phases exhibited a dot-like distribution, whereas PPAm-based phases showed a flake-like distribution, which is in high consistency with the surface morphology unveiled by the SEM results as discussed above. These results confirmed the more homogeneous surface coverage by the growth of the unique 1D phases compared to the conventional flake-like 2D structures.

The comparison of the PPAd and PPAm-based structures unveiled the significance of amidinium head group in forming a 1D perovskite phase that is easier to grow and cover the entire surface. By fixing the amidinium head group and introducing a different tethering unit (PAd), we further explored the functionality of the tethering chain. Although PAd and PPAd shared the identical head group of amidinium, significantly suppressed micro-inhomogeneity was observed for PPAd (Fig. 1B), indicating that the tail structure also regulated the molecular distribution and thus the lateral electronic energetics. Via the single crystal analysis of the perovskite phases based on these two structures, we found although both led to the formation of 1D perovskite structure (Supplementary Figs. 6, 14 and Supplementary Table 3), the Pb-I units were stacked in a more ordered manner in the in-plane direction for PPAd (Supplementary Fig. 15). The difference in the structure of the Pb-I frameworks can be attributed to the intermolecular interaction between the organic moieties. For PPAd, the Pb-I units were isolated by self-ordered organic cations via π-π interaction between the benzene rings. However, the alkyl chain in the PAd is much more flexible and cannot afford such stacking mode, and thus leading to a more

https://doi.org/10.1038/s41467-024-53953-4

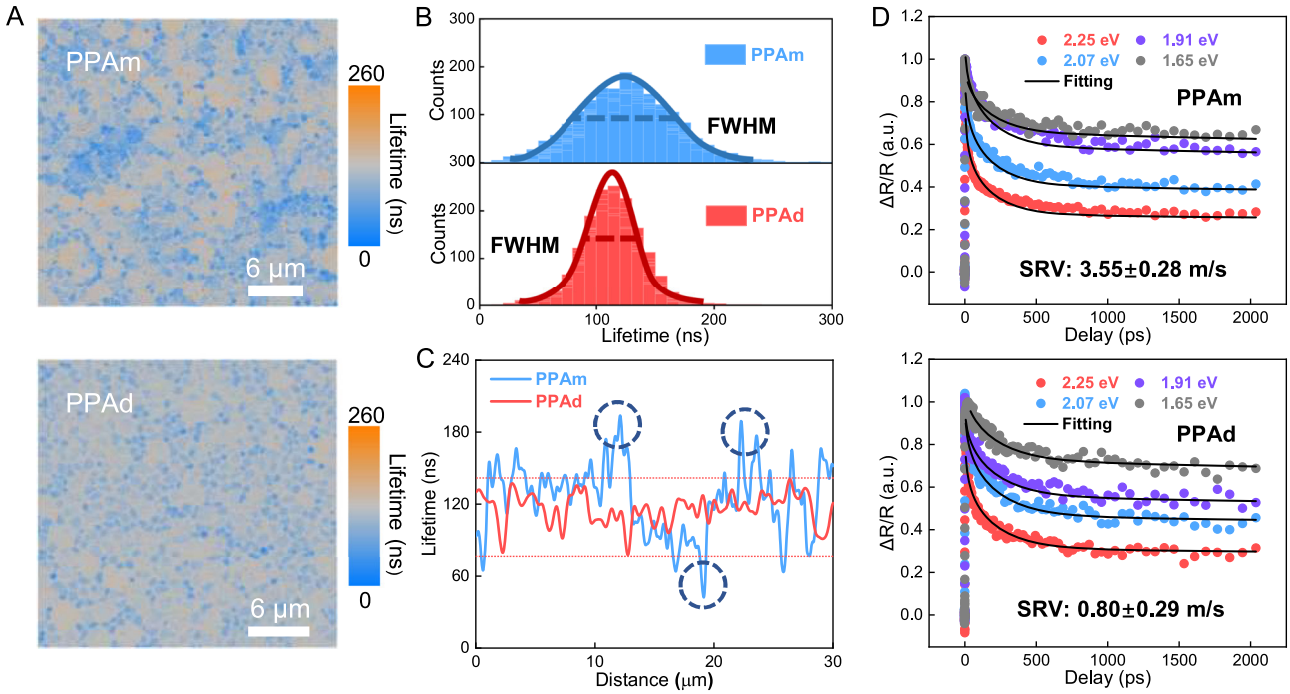

Fig. 2 | Lateral energetic inhomogeneity-induced charge carrier behaviors. **A** HTPL microscopic images of perovskite films treated with PPAm and PPAd. **B** Pixel-by-pixel statistical plots of the carrier lifetime extracted from the HTPL images for PPAm and PPAd. FWHM denotes the full-width half maximum (FWHM) of the lifetime distribution. **C** Line profiles of the carrier lifetime extracted from typical regions of the HTPL maps for PPAm and PPAd. **D** Surface-carrier kinetics pumped at 2.25, 2.07, 1.91, and 1.65 eV probed by TRS for perovskite films treated with PPAm and PPAd.

disordered structure. First-principle calculations also demonstrated that amidiniums with tethering benzene rings were more likely to arrange themselves in a stacked manner due to their increased stacking energies (Supplementary Fig. 16). As a result, PPAd, featuring both the amidinium head and the conjugated tail, delivered the most homogenous lateral energy landscape on a microscale among these molecules.

The difference in the microscale homogeneity was also reflected in the spatial distribution of the carrier lifetime. We statistically analyzed the carrier lifetimes of PPAm- and PPAd-treated perovskite samples, each dataset comprising 10 samples, derived from HTPL measurements. As illustrated in Fig. 2A and Supplementary Fig. 17, all PPAd-treated perovskite samples exhibited more homogeneous photoluminescence (PL) lifetimes compared to those treated with PPAm. These findings are consistent with the statistical analysis of the KPFM results presented in Supplementary Fig. 18. Pixel-by-pixel statistical plots of the carrier lifetime extracted from the HTPL images for these two cases are compared and displayed in Fig. 2B. While a negligible difference was observed in the average carrier lifetime of these two cases, PPAd exhibited a narrower distribution of the carrier lifetime than PPAm, showing improved homogeneity with PPAd. Line profiles of the carrier lifetime for PPAm and PPAd are compared and shown in Fig. 2C, better visualizing the higher spatial variation in the carrier lifetime with PPAm than with PPAd. The ensemble carrier lifetimes, indicated by the statistics of spatially averaged time-resolved photoluminescence (TRPL) spectra, were similar for PPAm and PPAd (Supplementary Fig. 19). The same trend held true for the distribution of the photoluminescence (PL) intensity collected simultaneously with the HTPL measurements (Supplementary Fig. 20), which further verified the improved lateral homogeneity with PPAd.

Although both PPAm and PPAd could comparably reduce the trap density, as indicated by the similar ensemble carrier lifetime, different degrees of lateral energetic homogeneity on the surface were induced. The lateral energy disorders could result in local electrical fields in the lateral directions influencing the surface carrier recombination dynamics. By using ultrafast transient reflection spectroscopy (TRS), we investigated the surface carrier dynamics for both cases. The timescale in the measurements was set as small as 2 ns to ensure negligible bulk recombination[33], which was usually on a timescale of microseconds. The TRS results revealed surface recombination velocities of 3.55 ± 0.28 and 0.80 ± 0.29 m/s for PPAm and PPAd, respectively (Fig. 2D). The relatively high surface recombination velocity for PPAm indicated that the local electrical fields induced by energetic heterogeneity were likely to increase the carrier recombination probability[34,35].

Film stability and degradation mechanisms

We then compared the stability of the as-fabricated perovskite films with PPAm and PPAd treatment via TRPL monitoring. The films were heated at 70 °C to accelerate their degradation, and the TRPL measurements were performed at different aging stages. As shown in Fig. 3A, the average carrier lifetime of the PPAm-treated film dropped swiftly over time. In contrast, the average carrier lifetime of the PPAd-treated film remained almost unchanged, suggesting improved film stability (Fig. 3B, C). To gain mechanistic insights into the lateral inhomogeneity-induced degradation of perovskite films, we performed in situ confocal PL mapping of the films during aging tests. The films were aged at 85 °C to accelerate their degradation while the real-time spatial PL information was collected. Figure 3D shows the maps of the PL peak position before and after 2 h of aging for PPAm- and PPAd-treated films. The PPAm-treated film showed a blueshift in the PL peak position, whereas the PPAd-treated film remained almost unchanged in the peak position. The corresponding line profiles in Fig. 3E better elucidated the different evolution of the PL peak position for these two cases, suggesting a local compositional variation with time for PPAm. The maps of the PL intensity depicted in Fig. 3F were extracted from the same location as the PL peak position. After 2 h of thermal aging, the PPAm-treated film, despite their decreased carrier lifetime indicated by HTPL, exhibited an unusual

https://doi.org/10.1038/s41467-024-53953-4

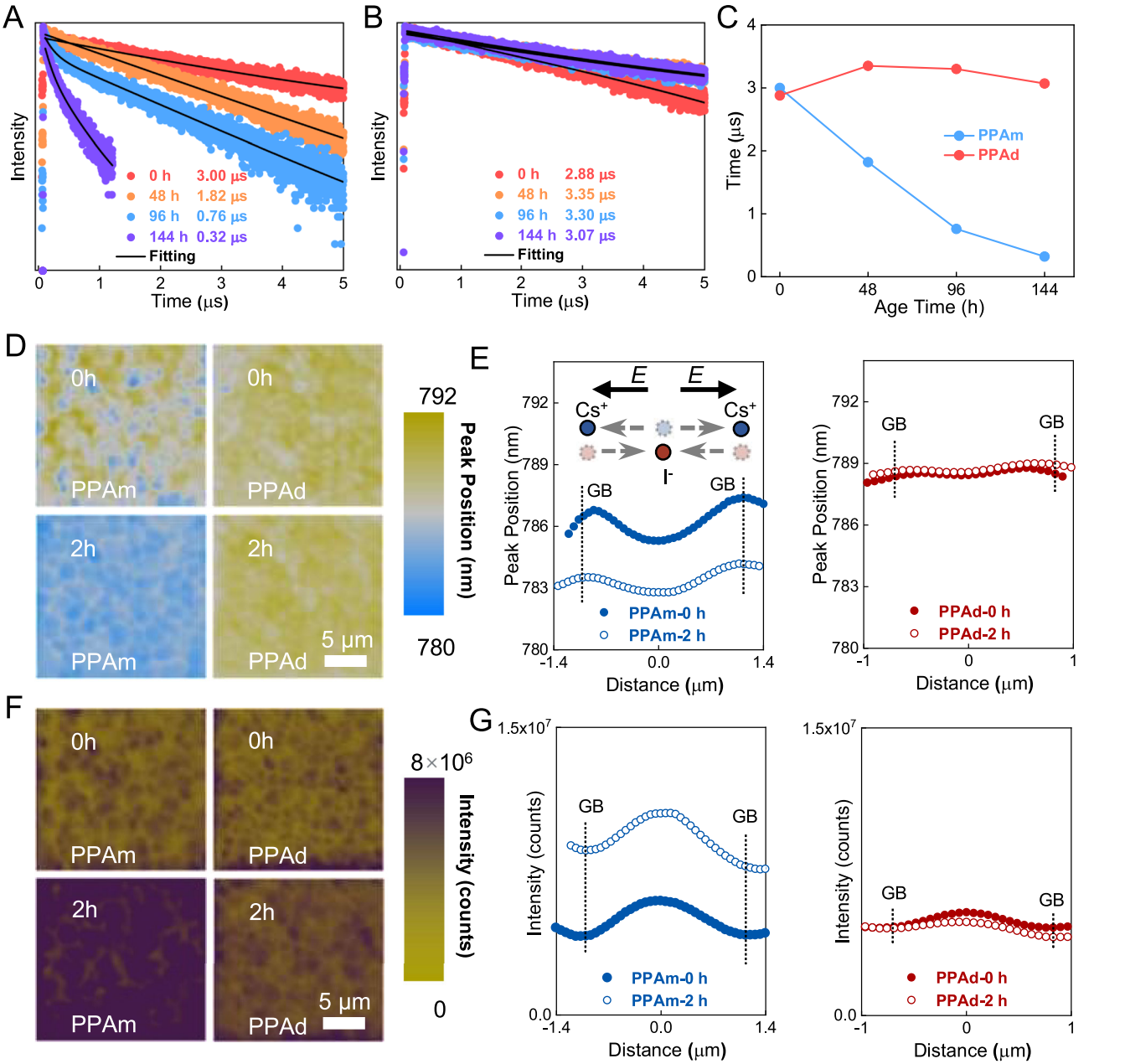

Fig. 3 | Film stability and degradation mechanisms. TRPL monitoring of perovskite films with **A** PPAm and **B** PPAd. **C** The evolution of average TRPL lifetime during the aging tests for perovskite films with PPAm and PPAd. **D** PL peak position maps via in situ PL mapping measurement for perovskite films during an accelerated aging test. **E** Line profiles of the PL peak position for PPAm and PPAd before and after aging. **F** Corresponding PL intensity maps for the perovskite films. **G** Line profiles of the PL intensity before and after aging.

increase in the PL intensity. The line profile of the PL intensity for a typical grain for PPAm and PPAd is shown in Fig. 3G, better illustrating the significant enhancement in the PL intensity over the grain with PPAm and only a slight decrease in the PL intensity with PPAd. We attributed the enhanced luminescence intensity with the peak blueshift in PPAm to the ion migration-induced generation of PbI_2. When excess PbI_2 was present in the perovskite film (Supplementary Fig. 21), we usually observed an unusual enhancement in the PL intensity accompanied by a blueshift in the peak position (Supplementary Fig. 22). This phenomenon was likely due to the passivation effect of PbI_2 on the perovskite surface[36]. However, the solar cell devices fabricated from these films containing excess PbI_2 always exhibited poor PCEs due to the limited carrier extraction capability (Supplementary Fig. 23).

The formation of PbI_2 was ascribed to ion migration facilitated by the local electrical field caused by lateral energetic heterogeneity. As the Fermi level of the surface of the grain region was higher than that of the grain boundary, the direction of the local electrical field was pointing from the grain to the grain boundary. As a result, the Cs^+ ions, which were among the most mobile cationic species in perovskites, tended to migrate from the grains to the grain boundaries. The I^- ions, featuring the lowest migration barriers among the anions, were driven from the grain boundaries to the grains during the aging test. The loss of A-site cations and the injection of halide anions expedited the formation of PbI_2 in the grain regions. Scanning electronic microscopy (SEM) images of the perovskite films before and after 2 h of aging tests are compared in Supplementary Fig. 24. After aging, PbI_2 crystals appeared on the surfaces of the grains, further

https://doi.org/10.1038/s41467-024-53953-4

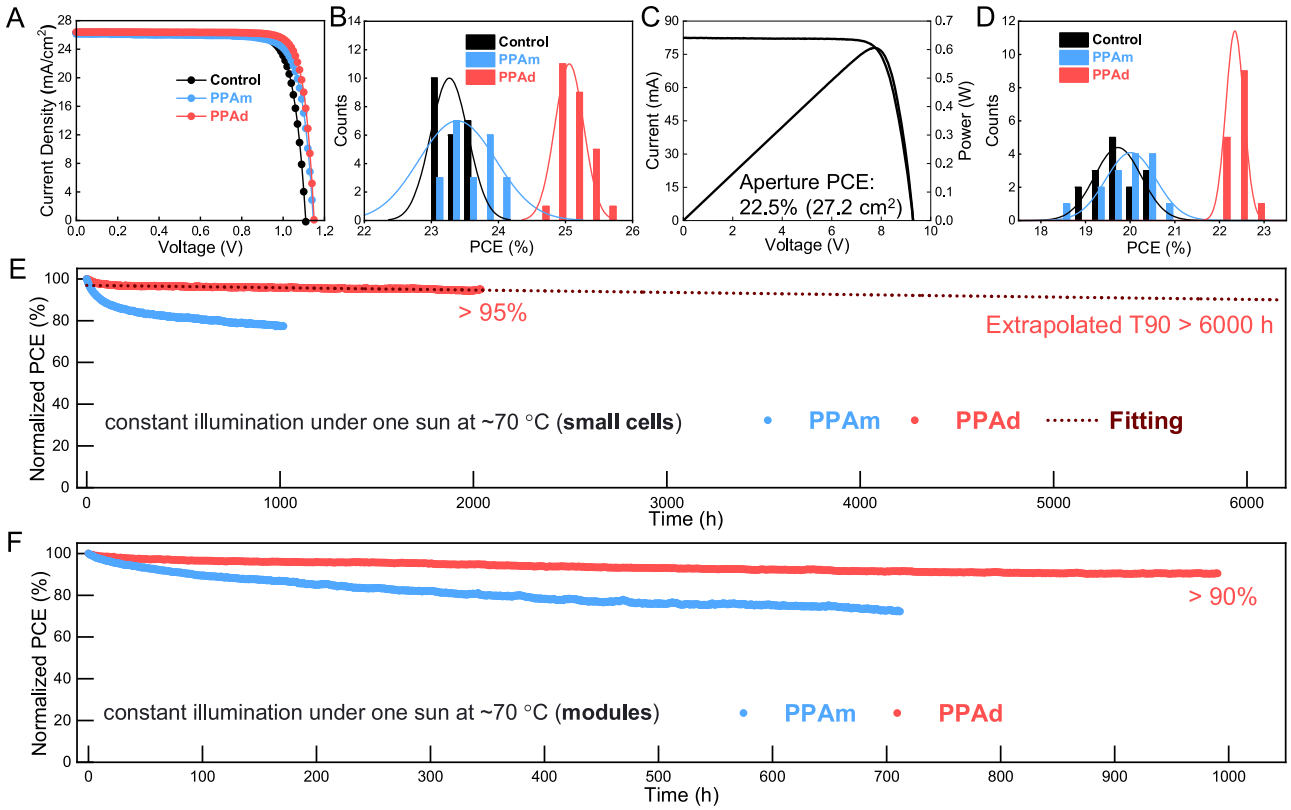

Fig. 4 | Device performance of perovskite solar cells and modules. A *J*–*V* curves and **B** PCE statistics of perovskite solar cell devices fabricated using one-step method with PPAm, PPAd, and the control. **C** Certified device performance of the perovskite solar module of an aperture area of 27.2 cm^2 fabricated with PPAd. **D** PCE statistics of perovskite solar modules fabricated with PPAm, PPAd, and the control. MPP tracking under continuous one-sun light soaking at ~70 °C of **E** perovskite solar cell and **F** perovskite solar modules.

verifying the local electrical field-facilitated ion migration and the excess PbI_2-resulted PL intensity enhancement with peak blueshift, as indicated above.

Characteristics of perovskite solar cells and modules

To assess the influence of lateral energetic homogeneity on the photovoltaic performance, we fabricated perovskite solar cells (0.1 cm^2) using the two-step method with a normal device architecture based on the surface passivation of PPAm and PPAd. Compared to the control devices without surface passivation, the passivated devices with either PPAm or PPAd showed improved PCEs, and the improvements in PPAd-based devices were higher than in PPAm (Supplementary Fig. 25). We also tested the performances of devices fabricated via one-step method. As shown in Fig. 4A, the PPAd treatment yielded a champion PCE of 25.5% with an open-circuit voltage (V_{oc}) of 1.15 V, a short-circuit current (J_{SC}) of 26.4 mA cm^{-2}, and a fill factor (FF) of 84.0%; the PPAm treatment resulted in a PCE of 24.2% with an open-circuit voltage (V_{oc}) of 1.15 V, a short-circuit current (J_{SC}) of 26.1 mA cm^{-2}, and a fill factor (FF) of 80.8%. In comparison, the control device showed a PCE of 23.8% with an open-circuit voltage (V_{oc}) of 1.11 V, a short-circuit current (J_{SC}) of 26.3 mA cm^{-2}, and a fill factor (FF) of 81.5%. The statistical comparison of the PCEs obtained from 20 devices for each condition is shown in Fig. 4B. Similar to the devices fabricated by the two-step method, although both the PPAm and PPAd treatments could increase the PCEs, PPAd led to a greater improvement than PPAm, demonstrating the universality. We attributed the superiority of PPAd over PPAm in PCE improvement to the suppressed surface carrier recombination, the probability of which would increase when lateral energetic inhomogeneity intensified. Moreover, the PPAm-based devices showed much reduced FF. We extracted the series resistance (R_s) and shunt resistance (R_{sh}) from the *J*–*V* curves of these devices (Supplementary Fig. 26). From the statistical results, the R_{sh} was not significantly changed, whereas the R_s in PPAm-based devices notably increased. Therefore, the decreased FF stemmed from the increased R_s, which could be attributed to the inhomogeneous PPAm surface layer leading to an increased contact resistance.

The lateral energy landscape was also found to be critical in affecting the performance of scaled-up devices. We assessed the photovoltaic performances of perovskite modules with an area of 27.2 cm^2 based on different surface treatments. While PPAm increased the champion aperture PCE of a perovskite module from 20.7% to 20.8% (Supplementary Fig. 27), the PPAd-based module achieved an even higher certified aperture PCE of up to 22.5% (V_{oc} = 9.29 V, I_{sc} = 83.2 mA, and FF = 79.2%, Fig. 4C). A certified steady-state PCE of 22.1% was obtained for the PPAd-based module (Supplementary Figs. 28 and 29). The statistical data collected from 15 solar modules demonstrated an average PCE of 19.7%, 20.0%, and 22.4% for the control, PPAm-, and PPAd-based modules, respectively (Fig. 4D), which was in agreement with the results from the small-area devices.

We examined the long-term stabilities of the perovskite small-area devices and modules under accelerated lifetime conditions by following the ISOS-L-1 consensus protocol. The PCEs of the devices were tracked at the maximum power point (MPP) under continuous one-sun light soaking at 70 °C. The small-area device treated with PPAd retained over 95% of its initial PCE after accelerated aging for ~2000 h, with a linear extrapolation to a T90 exceeding 6000 h (Fig. 4E, T90 denotes the time for a device to degrade to 90% of its maximum PCE), whereas the PPAm-treated device exhibited over 20% PCE loss at ~1000 h. The improved stability was mirrored in the perovskite solar modules. When aged at MPP under one-sun illumination at 70 °C, the

perovskite module with PPAd demonstrated a T90 of 1000 h (Fig. 4F), which surpassed other stability reports in perovskite solar modules (Supplementary Fig. 30). In contrast, the PPAm-treated module lost ~20% of its maximum PCE after ~300 h of the aging test. The control small-area device without any surface treatment exhibited an even shorter longevity than the PPAm-treated devices, with its PCE declining to 69% within 500 h. The large-area perovskite solar modules also experienced a significant reduction in PCE, dropping to 46% of its initial PCE within 300 hours. The substantially improved stability of perovskite modules with PPAd treatment further verified the above-mentioned film degradation mechanisms, highlighting the significance of lateral energetic micro-homogeneity in governing the longevity of scaled-up perovskite devices.

Discussion

While the most commonly used organic ammonium passivators could suppress the electronic traps and facilitate carrier transport in the vertical direction, they were found to cause micro-inhomogeneity in the surface lateral energetics, posing side effects on the device performance. Rationally designed organic amidinium passivators can deliver a flat energy landscape on a microscale. This lateral micro-homogeneity in energetics was found to be crucial to PSC performances, particularly in terms of device longevity and scale-up potential. While MA^+-headed organic ammonium surface passivators are prevailing to date, we anticipate that the FA^+-headed organic amidinium series reported in this work would come under the spotlight as research attention on FA-based perovskites has overwhelmed their MA-based counterparts. We believe this work will arouse great attention to the hitherto largely ignored lateral energetic micro-inhomogeneity caused by passivators, and provide important guidelines for the future design of effective passivators.

Methods

Materials

Solvents and chemicals were obtained commercially and used without further purification. N, N-dimethylformamide (DMF) (anhydrous, 99.8%), dimethyl sulfoxide (DMSO) (anhydrous, ≥99.9%), chlorobenzene (CB) (anhydrous, 99.8%), isopropanol (IPA) (anhydrous, 99.5%), water (ACS reagent), t-BP (99%), Li-TFSI (99.95% trace metals basis), PbI_2 (99.999%, perovskite grade), Cesium Iodide (CsI, 99.999%), silver (Ag) and gold (Au) were obtained from Sigma-Aldrich Inc. MACl (99%) and FAI was obtained from Great Cell. FK209 and Spiro-OMeTAD (99.8%) were obtained from Xi'an Polymer Light Technology Corp. Tin Oxide (SnO_2) nanoparticle (15 wt% in water) was obtained from Alfa-Aesar Inc. The materials used in the experiments of one-step method included: lead(II) iodide (PbI_2; 99.99%, TCI), tin(II) chloride dihydrate ($SnCl_2{\cdot}2H_2O$; 98%, Acros), tin(iv) chloride ($TiCl_4$; 99%, Sigma-Aldrich), hydrochloric acid (HCl; 37 wt% in H_2O, Sigma-Aldrich), methylammonium chloride (MACl, 99.99%, Greatcell solar), formamidinium iodide (FAI; 99.99%, Greatcell solar) N,N-dimethylformamide (DMF; 99.8%, Sigma-Aldrich), dimethyl sulfoxide (DMSO; 99.9%, Sigma-Aldrich), 2-propanol (99.5%, Sigma-Aldrich), chlorobenzene (99.8%, Sigma-Aldrich), Spiro-OMeTAD (Borun Tech.), 4-tert-butylpyridine (tBP; Sigma-Aldrich), bis(trifluoromethane)sulfonimide lithium salt (Li-TFSI; 99.95%, Sigma-Aldrich), FK209 Co(III) TFSI salt (Sigma-Aldrich, acetonitrile (ACN; 99.8%, Sigma-Aldrich)), 1-Pentylamine hydrochloride (PAm, 98%, TCI), 1-Pentanimidamide hydrochloride (PAd, 98%, Bldpharm), 3-Phenylpropionamidine hydrochloride (PPAd, 98%, Bide Pharmatech), 3-Phenylpropylamine hydrochloride (PPAm) was synthesized in our laboratory. Initially, 5 mL of phenylpropylamine was dissolved in 50 mL of ethanol, and the solution was stirred in an ice-water bath. Subsequently, 4 mL of hydrochloric acid was added gradually, and the reaction was allowed to proceed overnight. The resulting precipitate was washed three times with ether and then dried in an oven at 60 °C overnight.

Device fabrication

(1) Fabrication of perovskite solar cells by two-step method. For the perovskite layer made by the two-step method, perovskite solar cells were fabricated with the following structure: indium tin oxide (ITO)/SnO_2/$FA_{0.95}Cs_{0.05}PbI_3$/Spiro-OMeTAD/Ag or Au. The ITO glass was pre-cleaned in an ultrasonic bath of acetone and isopropanol and treated in ultraviolet-ozone for 20 min before use. A thin layer (ca. 30 nm) of SnO_2 was spin-coated onto the ITO glass and baked at 165 °C for 35 min. SnO_2 solution was diluted in water (V_{SnO2}:V_{H2O} = 1:4) before spin-coating. After cooling down to room temperature, the glass/ITO/SnO_2 substrates were transferred into a nitrogen glove box. The PbI_2 solution was prepared by dissolving 1.4 M PbI_2 and 0.07 M CsI into 1 mL DMF/DMSO mixed solvent (v/v 94/6). The FAI solution for the control film was prepared by dissolving 80 mg FAI with a small amount of MACl (13 mg) into 1 mL IPA. To fabricate the perovskite layer, the PbI_2 solution was spin-coated on the substrate at 1500 rpm for 40 s, and then, the FAI solution was spin-coated on the PbI_2 film at 1800 rpm for 40 s, followed by pre-annealing inside the glove box at 90 °C for 1 min and annealing outside the glove box at 150 °C for 10 min with 30–40% humidity. A 5 mM concentration of PAm, PAd, PPAm, and PPAd in IPA solvent was used to treat the as-prepared perovskite films, followed by annealing the films at 100 °C for 1 minute. The Spiro-OMeTAD solution [60 mg Spiro-OMeTAD in 700 μL CB with 25.5 μL t-BP, 15.5 μL Li-TFSI (520 mg/mL in ACN) and 12.5 μL FK209 (375 mg/mL in ACN)], was spun onto the perovskite film as a hole conductor. The devices were completed by evaporating 100 nm gold or silver in a vacuum chamber (base pressure, 5×10^{-4} Pa) and the aperture area of the device is 0.1 cm^2, designated by the shadow mask.

(2) Fabrication of perovskite solar cells by one-step method. The device with an architecture of FTO glass/compact TiO_2 layer (c-TiO_2)/compact SnO_2 layer, (c-SnO_2)/$Cs_{0.05}MA_{0.05}FA_{0.9}PbI_3$ (PVK)/spiro-OMeTAD (HTM)/Au structure was fabricated. The patterned FTO substrate (Asahi FTO glass, 12–13 Ω cm^{-2}) was sequentially cleaned with detergent (5% Hellmanex in water), deionized water, acetone, and isopropanol in the ultrasonic bath for 30 min, respectively. The FTO substrate was then further cleaned with Ultraviolet-Ozone surface treatment for 15 min. The compact TiO_2 (c-TiO_2) and SnO_2 layer were sequentially deposited on the clean FTO substrate by the chemical bath deposition (CBD) method. The substrate was annealed on a hot-plate at 190 °C for 60 min. The perovskite precursor solution (1.4 M) was prepared by adding 645.4 mg of PbI_2, 216.7 mg of formamidium iodide (FAI), 33.1 mg of methylammonium chloride (MACl), 11.1 mg of methylammonium iodide (MAI), and 11.8 mg of CsCl into 200 μL of N, N′-dimethylsulfoxide (DMSO) and 800 μL of dimethyformamide (DMF) mixture. The solution was then stirred for 2 h at 60 °C. After UV-ozone treatment of the substrates for 15 min, the perovskite precursor solution was spin-coated onto the surface of the FTO/c-TiO_2/c-SnO_2 substrate at 1000 rpm for 10 s, accelerated to 5000 rpm for 5 s and maintained at this speed for 20 s. This process was carried out in an N_2 filled glove box. Then, the substrate was placed in a homemade rapid vacuum drying equipment, as previously reported[37]. After pumping for 20 s, a brown, transparent perovskite film with a mirror-like surface was obtained. The fresh perovskite layer was annealed at 100 °C for 1 h and then at 150 °C for 10 min. Afterward, A 5 mM concentration of PPAm, and PPAd in IPA solvent was used to treat the as-prepared perovskite films, followed by annealing the films at 100 °C for 1 minute. A hole transport layer was deposited on the perovskite film by depositing a doped spiro-OMeTAD solution at 3000 rpm for 30 s. The doped spiro-OMeTAD solution was prepared by dissolving 105 mg of spiro-OMeTAD and 41 μL of 4-tert-butylpyridine in 1343 μL of chlorobenzene with additional 25 μL of bis(trifluoromethane)sulfonimide lithium salt solution (517 mg/mL in acetonitrile) and 19 μL of cobalt-complex solution (376 mg/mL in acetonitrile). Finally, a ~70-nm-thick gold layer was evaporated on the spiro-OMeTAD layer as the back electrode and the aperture area of the certified device is 0.06 cm^2.

(3) Fabrication of perovskite mini-modules. Perovskite solar modules, with 8 sub-cells connected in series, were fabricated on FTO glass substrates with a size of 6.5 × 7.0 cm^2. The series interconnection of the module was realized by P1, P2, and P3 lines, which were patterned using a laser scribing system with a 1064 nm and a power of 20 W (Trotec). The FTO substrate was pre-patterned for P1 (a width of 40 μm) by means of 60% laser power under a speed of 300 mm/s with a frequency of 65 kHz and pulse width of 120 ns. The subsequent processes for the preparation of c-TiO_2/c-SnO_2 substrates are the same with the small-area device procedures. Besides, the perovskite precursor deposition and fabrication procedures were also similar to that of the small-size solar cells except for the concentration of perovskite precursor. 1.1 M of perovskite precursor was employed to do the perovskite layer by using spin-coated method and custom-made gas-induced pump method. The perovskite precursor was spin-coated on the c-TiO_2/c-SnO_2 substrates, which are similar with those of the small-size devices. The perovskite films were annealed at 100 °C for 1 h and 150 °C for 10 min. Afterward, A 5 mM concentration of PPAm, and PPAd in IPA solvent was used to treat the as-prepared perovskite films, followed by annealing the films at 100 °C for 1 min. After cooling down to room temperature, the Spiro-OMeTAD layer are similar to those of the small-size devices. The P2 lines (a width of 100 μm) were patterned before the Au evaporation process step with an average laser power of 15% under a speed of 1000 mm/s and frequency of 65 kHz for pulse duration of 120 ns. When a 70-nm-thick Au layer was deposited, the P3 line (a width of 60 μm) was fabricated under the same scribing condition as the P2 line. The distance between P1 and P3 was around 240 μm, and a geometric fill factor (GFF) was around 96.0%.

Stability test

The devices for stability test were fabricated using the method mentioned above with a structure of FTO/SnO_2/perovskite/PTAA/MoO_x/ITO/Au. The devices were encapsulated by a glass-glass encapsulation technology combined with an edge seal (UV Curing Sealant, Three bond 3035B) to seal the device under UV light illumination (LED flood lamp, DELOLUX 20). First, the edge of the device was cleared by laser. An indium solder was soldered on the FTO and Au electrodes on the edge of the substrate. Then, a glass was put on the top of the Au layer of the device. A light-curing sealant was deposited on the edges of the glass to fully cover the gap between the top glass and device. Finally, a UV light was employed to induce the cross-linking in sealant with a glass under a 25% maximum power for 120 s in the glove box. For the accelerated degradation test, the encapsulated devices were kept in a thermo-hygrostat (GP/TH-150, SH Guangpin test Equipment Manufacturing Co., Ltd), which was set under 30 ± 5% relative humidity at ~70 °C. The devices were measured by an electronic system using a 22-bit delta-sigma analog-to-digital converter. A reference Si photodiode was placed in the neighbor of devices to record the light intensity. The long-term stability tests were measured at the maximum power point (MPP) condition using a MPP tracking algorithm under 1 Sun illumination according to ISOS-L-3 protocol.

Device characterization

J–V characteristics of photovoltaic cells were taken using a Keithley 2400 source measure unit under a simulated AM 1.5 G spectrum, with an Oriel 9600 solar simulator. Typically, the small-size devices were measured in reverse scan (1.20 ⟶ 0 V, step 0.01 V). The modules were measured in reverse scan (from 9.5 to 0 V) under a constant scan speed of 100 mV/s with a step of 50 mV. For the measurement of high-efficiency devices, an anti-reflection film was applied on the surface of devices. All the devices were measured without pre-conditioning, such as light-soaking and applied a bias voltage. Steady-state power conversion efficiency was calculated by measuring stabilized photocurrent density under a constant bias voltage. The incident photon-to-current conversion (IPCE) values were confirmed as a function of wavelength from 300 to 900 nm (IQE200B, Oriel) for devices without bias light. In order to evaluate the optical properties of the device, no anti-reflection layer was used. External quantum efficiencies were measured using an integrated system (Enlitech) and a lock-in amplifier with a current preamplifier under short-circuits' condition.

Materials characterization and spectroscopic investigation

UV-vis absorption spectra of the perovskite films were obtained using a Shimadzu UV-VIS-NIR (UV3600Plus + UV2700) equipped with an integrating sphere, in which monochromatic light was incident to the substrate side. For TRPL measurement, the sample was excited with a picosecond pulsed diode laser (Pico-quant LDH 450), with a ~70 ps pulse width and 10 MHz repetition rate, focused on sample with a 100x objective (NA = 0.90). The PL signal was acquired through the TCSPC strobelock system. The total instrument response function (IRF) for the PL decay was less than 200 ps, and the temporal resolution was less than 30 ps. The energy laser for TRPL measurements was 5 mW. XRD experiments were performed on sealed-tube Cu X-ray source, equipped with 1D LynxEye detector. GIWAXS measurements were conducted on the BL14B beamline at the Shanghai Synchrotron Radiation Facility (SSRF). Scanning electronic microscopy was measured via Gemini 450. The GIWAXS 2D images were collected by MarCCD225 detector. The wavelength of the X-ray for testing was kept at 1.24 Å. The light incident angle of each sample was kept at 0.15° to detect diffraction signals at different depths of perovskite film with an exposing time of 50 s. Kelvin probe force microscope (KPFM) was measured by Environmental Atomic Force Microscopy (Cypher ES). The KPFM measurements were conducted on perovskite samples housed within a sealed chamber, as illustrated in Supplementary Fig. 31, which was purged with nitrogen gas. This ensured that the KPFM measurements remained unaffected by external stimuli such as oxygen and moisture. In situ photoluminescence (PL) and mapping were measured on alpha 300 R (WITec GMBH, Germany) confocal TA Raman system. A diode-pumped solid-state laser (532 nm, cobalt Laser) was focused on samples with a diffraction-limited beam size of 590 nm by a 50x long-focus objective (NA = 0.55). The perovskite film sample was pumped into a vacuum chamber for 10 minutes to remove water and oxygen, and heated at 70 °C. The collected PL signal was dispersed by UHTS 600 mm spectrometer and detected using an electron-magnified charge-coupled-device (EMCCD) thermoelectrically cooled to −60 °C. Ultrafast PL imaging was running with a 200 nm step size and 10 ms integration time. High-resolution time-resolved photoluminescence (HTPL) mapping was taken using a Leica Stellaris 8 FALCON inverted microscopic system. A Leica 63× oil immersion objective with numerical aperture of 1.40 was used for the measurement. Samples were placed on a cover glass with thickness of 0.17 mm with the front surface downward during the measurement. A 488-nm laser line (FWHM ~ 1 nm, repetition rate 2.5 MHz) picked from a supercontinuum laser source was used to excite the perovskite samples. The point spread function of the microscopic system was 212.6 nm FWHM. The excitation power was kept ~0.11 μW at 2.5 MHz, corresponding to an incident photon flux of 7.612 × 10^{13} photons/cm^2 per pulse. The PL photons emitted by the samples with wavelengths of 750–850 nm were collected by the same objective and were detected by a GaPAs-based HyD-R single-photon detector. The minimum temporal resolution of the system was ~97 ps. The XY-plane scanning for the PL intensity and lifetime imaging within 20 μm × 20 μm in size and 1024 × 1024 pixels in resolution was realized by a high-speed Galvo scanning system. The results were analyzed and processed using LASX analysis software (Leica). For the HTPL measurements by laser repetition rate of 1.0 MHz, PL intensity and lifetime images were acquired using a PicoQuant MicroTime 200 confocal fluorescence microscope. The sample was placed front surface downward on a cover glass (thickness 0.17 mm) and imaged using a 100x oil

immersion objective (Olympus, NA = 1.45). The excitation light source was a 510 nm laser (PicoQuant, LDH-D-C-520, repetition rate set to 1 MHz), with the excitation intensity fixed at ~0.02 μW. The photons passed through a 519 nm lang pass filter and were detected by a SPAD detector (Excelitas Technologies). The luminescence intensity and lifetime information were collected simultaneously. The scanning speed was set to 200 μs/point, and frames were accumulated until reaching 1000 photons/pixel. The image size was set to 10 × 10 μm, and the resolution was set to 256 × 256 pixels. The data were analyzed and processed using SynPhoTime 64 software. A pump–probe spectrometer performed transient reflectance (TR) spectroscopy. A femtosecond laser based on Yb:KGW regenerative amplifier (Pharos, Light Conversion; ~190 fs) generated a 1030 nm pulse at a 100 kHz repetition rate. Transmission Fourier transform infrared (FTIR) spectroscopy was obtained using FT/IR-6100 (Jasco). UPS measurements were carried out to determine the work function and the position of valence band maximum of materials. A He discharge lamp, emitting ultraviolet energy at 21.2 eV, was used for excitation. All UPS measurements were performed using standard procedures with a −10 V bias applied between the samples and detectors. Clean gold was used as a reference. ToF-SIMS depth-profile analysis was performed using a PHI NanoTOF III instrument (ULVAC-PHI, Inc.), where a 3 kV Ar ion beam was used for erosion and a 25 keV Bi^+ pulsed primary ion beam was used for the analysis. The area of analysis was 100 × 100 μm^2 while the sputtering area was 400 × 400 μm^2. After heating and complete dissolution, the solution was put into a muffle furnace for cooling and high-purity halide perovskite single crystal was obtained after around 48 h. Transmission Fourier transform infrared (FTIR) spectroscopy was obtained using FT/IR-6100 (Jasco). The single crystal was grown via slow cooling crystallization method. For PAd-based single crystal perovskite, 0.73 mmol PAd, and 0.65 mmol PbI_2 were added into 1 mL hydriodic acid (HI, 57 wt%, TCI) and 0.1 mL hypophosphorous acid (H_3PO_2, J&K Scientific). For PPAd-based single crystal perovskite, 0.16 mmol PPAd, and 0.65 mmol PbI_2 were added into 1 mL HI and 0.1 mL H_3PO_2. For PPAm-based single crystal perovskite, 0.16 mmol PPAm, and 0.65 mmol PbI_2 were added into 1 mL HI and 0.1 mL H_3PO_2. After heating and complete dissolution, the solution was cooled in a muffle furnace, resulting in the formation of high-purity halide perovskite single crystals within approximately 48 h. SEM was carried out on the Field Emission Environment Scanning Electron Microscope of Quattro S. XPS measurements were carried out on an XPS (ThermoFisher ESCALAB Xi+). An Al Kα (1486.6 eV) X-ray was used as the excitation source. Transient absorption measurements were performed by a pump–probe spectrometer (TA-100, Time-Tech spectra).

DFT calculations

We conducted first-principles calculations based on the density functional theory (DFT) with a plane-wave basis set and the projected augmented wave (PAW) method using the VASP package[38,39]. We utilized the Perdew–Burke–Ernzerhof (PBE) functional with a generalized-gradient approximation for the exchange-correlation functional in both the geometry optimization and self-consistent field calculations[40]. To conduct the geometry optimizations, we used a 4 × 4 × 1 Γ-centered k-mesh and a plane wave basis with an energy cutoff of 400 eV. We allowed the atomic positions and cell volumes to relax using a conjugate gradient algorithm until all residual forces were less than 0.02 eV/Å. We also included a vacuum slab with a thickness of 10–15 Å between the periodic slab-molecule structure in the z direction.

Reporting summary

Further information on research design is available in the Nature Portfolio Reporting Summary linked to this article.

Data availability

Crystallographic data for the single crystal reported in this article have been deposited at the Cambridge Crystallographic Data Center (CCDC), with deposition numbers 2387181, 2387182, and 2387180 corresponding to (PPAd)Pb_2I_6, (PPAm)Pb_3I_{10}, and (PAd)PbI_3 respectively. These crystallographic data can be obtained free of charge via https://www.ccdc.cam.ac.uk/structures/. The main data generated in this study are provided in the Supplementary Information/Source data file. All other data supporting the findings of this study are available from the corresponding authors on request. Source data are provided with this paper.

References

1. Chen, H. et al. Quantum-size-tuned heterostructures enable efficient and stable inverted perovskite solar cells. *Nat. Photonics* **16**, 352–358 (2022).
2. Shao, Y., Yuan, Y. & Huang, J. Correlation of energy disorder and open-circuit voltage in hybrid perovskite solar cells. *Nat. Energy* **1**, 15001 (2016).
3. Zhang, F. et al. Metastable Dion-Jacobson 2D structure enables efficient and stable perovskite solar cells. *Science* **375**, 71–76 (2022).
4. Duan, X. et al. Controlling crystal growth via an autonomously longitudinal scaffold for planar perovskite solar cells. *Adv., Mater.* **32**, 2000617 (2020).
5. Kim, M. et al. Methylammonium chloride induces intermediate phase stabilization for efficient perovskite solar cells. *Joule* **3**, 2179–2192 (2019).
6. Lee, J.-W. et al. A bifunctional Lewis base additive for microscopic homogeneity in perovskite solar cells. *Chem* **3**, 290–302 (2017).
7. Li, N. et al. Liquid medium annealing for fabricating durable perovskite solar cells with improved reproducibility. *Science* **373**, 561–567 (2021).
8. Correa-Baena, J.-P. et al. Homogenized halides and alkali cation segregation in alloyed organic-inorganic perovskites. *Science* **363**, 627–631 (2019).
9. Bai, Y. et al. Initializing film homogeneity to retard phase segregation for stable perovskite solar cells. *Science* **378**, 747–754 (2022).
10. Jiang, Q. et al. Compositional texture engineering for highly stable wide-bandgap perovskite solar cells. *Science* **378**, 1295–1300 (2022).
11. Min, H. et al. Efficient, stable solar cells by using inherent bandgap of α-phase formamidinium lead iodide. *Science* **366**, 749–753 (2019).
12. Wang, Y. et al. The role of dimethylammonium iodide in $CsPbI_3$ perovskite fabrication: additive or dopant? *Angew. Chem. Int. Ed.* **58**, 16691–16696 (2019).
13. Jeon, N. J. et al. A fluorene-terminated hole-transporting material for highly efficient and stable perovskite solar cells. *Nat. Energy* **3**, 682–689 (2018).
14. Tan, S. et al. Stability-limiting heterointerfaces of perovskite photovoltaics. *Nature* **605**, 268–273 (2022).
15. Xue, J. et al. Reconfiguring the band-edge states of photovoltaic perovskites by conjugated organic cations. *Science* **371**, 636–640 (2021).
16. Zhou, H. et al. Interface engineering of highly efficient perovskite solar cells. *Science* **345**, 542–546 (2014).
17. Jiang, Q. et al. Surface reaction for efficient and stable inverted perovskite solar cells. *Nature* **611**, 278–283 (2022).
18. Jiang, Q. et al. Surface passivation of perovskite film for efficient solar cells. *Nat. Photonics* **13**, 460–466 (2019).
19. Yang, G. et al. Stable and low-photovoltage-loss perovskite solar cells by multifunctional passivation. *Nat. Photonics* **15**, 681–689 (2021).
20. Chen, P., Bai, Y. & Wang, L. Minimizing voltage losses in perovskite solar cells. *Small Struct.* **2**, 2000050 (2021).

21. Xue, J., Wang, R. & Yang, Y. The surface of halide perovskites from nano to bulk. *Nat. Rev. Mater.* **5**, 809–827 (2020).
22. Peng, W. et al. Reducing nonradiative recombination in perovskite solar cells with a porous insulator contact. *Science* **379**, 683–690 (2023).
23. Crossland, E. J. W. et al. Mesoporous TiO2 single crystals delivering enhanced mobility and optoelectronic device performance. *Nature* **495**, 215–219 (2013).
24. Kim, H.-S. et al. Lead iodide perovskite sensitized all-solid-state submicron thin film mesoscopic solar cell with efficiency exceeding 9%. *Sci. Rep.* **2**, 591 (2012).
25. Azmi, R. et al. Damp heat–stable perovskite solar cells with tailored-dimensionality 2D/3D heterojunctions. *Science* **376**, 73–77 (2022).
26. Hui, W. et al. Stabilizing black-phase formamidinium perovskite formation at room temperature and high humidity. *Science* **371**, 1359–1364 (2021).
27. Turren-Cruz, S.-H., Hagfeldt, A. & Saliba, M. Methylammonium-free, high-performance, and stable perovskite solar cells on a planar architecture. *Science* **362**, 449–453 (2018).
28. Li, H. et al. Additive engineering to grow micron-sized grains for stable high efficiency perovskite solar cells. *Adv. Sci.* **6**, 1901241 (2019).
29. Liu, C. et al. Improving the performance of perovskite solar cells via a novel additive of N,1-fluoroformamidinium iodide with electron-withdrawing fluorine group. *Adv. Funct. Mater.* **31**, 2010603 (2021).
30. Kim, J.-H. et al. Effect of functional groups in passivating materials on stability and performance of perovskite solar cells. *J. Mater. Chem. A* **11**, 15014–15021 (2023).
31. Chen, S. et al. Control of the surface disorder by ion-exchange to achieve high open-circuit voltage in $HC(NH_2)_2PbI_3$ perovskite solar cell. *Small Methods* **5**, 2101079 (2021).
32. Liu, L. et al. Multi-site intermolecular interaction for in situ formation of vertically orientated 2D Passivation layer in highly efficient perovskite solar cells. *Adv. Funct. Mater.* **33**, 2303038 (2023).
33. Yang, Y. et al. Top and bottom surfaces limit carrier lifetime in lead iodide perovskite films. *Nat. Energy* **2**, 16207 (2017).
34. Wang, J. et al. Reducing surface recombination velocities at the electrical contacts will improve perovskite photovoltaics. *ACS Energy Lett.* **4**, 222–227 (2019).
35. Wang, R. et al. Unraveling the surface state of photovoltaic perovskite thin film. *Matter* **4**, 2417–2428 (2021).
36. Jiang, Q. et al. Planar-structure perovskite solar cells with efficiency beyond 21. *Adv. Mater.* **29**, 1703852 (2017).
37. Gao, L.-L. et al. Preparation of flexible perovskite solar cells by a gas pump drying method on a plastic substrate. *J. Mater. Chem. A* **4**, 3704–3710 (2016).
38. Kresse, G. & Furthmüller, J. Efficiency of ab-initio total energy calculations for metals and semiconductors using a plane-wave basis set. *Comput. Mater. Sci.* **6**, 15–50 (1996).
39. Kresse, G. & Hafner, J. Ab initio molecular dynamics for liquid metals. *Phys. Rev. B* **47**, 558 (1993).
40. Komsa, H.-P., Broqvist, P. & Pasquarello, A. Alignment of defect levels and band edges through hybrid functionals: effect of screening in the exchange term. *Phys. Rev. B* **81**, 205118 (2010).

Acknowledgements

All the authors thank Dr. Zhong Chen and from Instrumentation and Service Center for Molecular Sciences, and Dr. Lin Liu from Instrumentation and Service Center for Physical Sciences (ISCPS) at Westlake University for the assistance in the characterizations. J.X. and R.W. acknowledge the grant (LD22E020002, LD24E020001) by Natural Science Foundation of Zhejiang Province of China. J.X. acknowledges the financial support by Shanxi-Zheda Institute of Advanced Materials and Chemical Engineering (2021SZ-FR006). J.X. acknowledges the grant by the National Natural Science Foundation of China (grant no. 62274146) and the grant (LR24F040001) by Natural Science Foundation of Zhejiang Province of China. R.W. acknowledges the support of Key R&D Program of Zhejiang (2024SSYS0061) and the support of the Research Center for Industries of the Future.

Author contributions

J.X., R.W., and P.S. conceived the idea. P.S. and D.J. did the fabrication of perovskite films and devices, and did the data analysis under the supervision of R.W. and J.X., B.D., and Y.D. fabricated the solar modules under the supervision of M.N. M.O. carried out the theoretical calculations under the supervision of C.D. and I.Y., X.Z., Y.T., Z.S., J.Xu, K.Z., R.L., C.W., L.T., J.S., Y.C., X.M., and S.Z. assisted with the device fabrication and characterizations. Y.L. helped to grow single crystals under the supervision of E.S. L.X. assisted with the film characterizations. D.Y. provides helpful discussion. J.X. wrote the manuscript and P.S. wrote the response. All the authors discussed the results and commented on the manuscript.

Competing interests

The authors declare no competing interests.

Additional information

Supplementary information The online version contains supplementary material available at https://doi.org/10.1038/s41467-024-53953-4.

Correspondence and requests for materials should be addressed to Yong Ding, Mohammad Khaja Nazeeruddin, Rui Wang or Jingjing Xue.

Peer review information *Nature Communications* thanks the anonymous, reviewers for their contribution to the peer review of this work. A peer review file is available.